Robust adaptive control of uncertain electric ground vehicles using $\mathcal{L}1$ theory and projection algorithm

Abstract

In this study, a robust adaptive control strategy using a $\mathcal{L}1$ theory is applied to fulfil the motion control of a four-wheel electric vehicle. The dynamic model includes longitudinal, and lateral velocity and yaw rate. To develop the proposed control strategy, the vehicle dynamics are decomposed into linear and non-linear components. The linear part is controlled by fine-tuned state feedback, with its steady-state error addressed by a feedforward control block. The nonlinear part is addressed based on nonlinear adaptive laws and $\mathcal{L}1$ theory to mitigate adverse effects on the linear dynamics, unwanted parameter changes, and external disturbances. An essential component of the proposed approach is the incorporation of a reference model that dictates the desired system responses. A projection algorithm is used to instantly estimate the nonlinear part of the vehicle dynamics. The performance of the closed-loop system is thoroughly evaluated over a range of vehicle manoeuvres, assessing factors such as steady-state accuracy, transient response and power consumption. In addition, the effectiveness of the proposed method is compared with conventional model reference adaptive control and a recent robust control approach, particularly in terms of robustness to uncertainties inherent in the non-linear aspects of vehicle dynamics.

Keywords: Electric vehicle, $\mathcal{L}1$ adaptive control, projection algorithm, model uncertainty, motion tracking.

1 Introduction

Electric Vehicles (EVs) are becoming increasingly important for sustainable transportation. Compared to conventional internal combustion engine vehicles, EVs have numerous benefits such as reduced greenhouse gas emissions, improved energy efficiency, and lower noise pollution [1]. With many countries aiming to phase out fossil-fuel vehicles, EVs are expected to become a major part of the global fleet [2]. However, there are still challenges around battery costs, charging infrastructure and driving range that need to be addressed.

Advanced modelling and control of EVs is crucial to improve their performance and make them more competitive. Sophisticated models account for complex EV powertrain components such as motors, batteries, and power electronics [3]. Control systems leverage these models to optimize efficiency, increase driving range [4], and enable different energy management systems [5]. Developing robust integrated models and implementing them with advanced adaptive control strategies is an important area of ongoing research for EV engineers and scientists.

Various advanced control strategies have been applied to EVs to optimize their performance. Sliding Mode Control (SMC) provides robustness against disturbances and parameter variations for EV traction systems. It includes a nonlinear control term to maintain internal stability and a switching term to ensure robustness. An Adaptive backstepping SMC is introduced in [6] to improve vehicle manoeuvrability and stability through Torque Vectoring Control (TVC). Backstepping control is a recursive control system based on Lyapunov theory. The TVC adjusts the torque applied to individual wheels to optimize vehicle dynamics. Backstepping technique is also used in [7] to manage both the overall speed of the car and the speed of each wheel. It uses a detailed model that considers factors like wind resistance, tire rolling, and grip on the road.

A variable structure control for a hybrid EV incorporating a fuel cell, supercapacitor, and battery is introduced in [8]. An advanced control system is proposed in [9] for autonomous EVs that employs second-order SMC and nonlinear disturbance observer to enhance path-following precision and stability. A disturbance observer is an inner-loop feedback function that aims to reject the external disturbances. In [10], A combination of fuzzy logic and super twisting SMC are used to optimize energy storage. Super-twisting SMC overcomes the variations caused by the switching term. An adaptive fuzzy SMC system for the regenerative braking of EVs seeks to optimize energy recovery and braking effectiveness [11]. This method dynamically adjusts its parameters based on real-time conditions. A SMC approach is applied to the anti-lock braking system of EVs [12] to optimize the braking system's response.

A disturbance observer-based SMC to optimize energy interaction between multiple vehicles in EV networks is developed in [13]. In [14], a SMC dynamically adjusts the distribution of torque and steering to optimize stability and manoeuvrability. An integration of Active Front Steering (AFS), SMC, and an extreme learning algorithm is proposed in [15] for improved stability and adaptability of EVs. AFS adjusts the steering wheel angle by superimposing an additional angle. In [16], an adaptive dynamic SMC system with an extended state observer is employed for throttle control in EVs. This system regulates the power sent from the battery to the electric motor. A modified adaptive super twisting sliding mode observer with moving-average filter phase-locked loop enhanced control of EVs [17]. This method synchronizes the phase and frequency of the output signal with a reference signal.

Although SMC-based methods are easy to implement and provide closed-loop robustness, they typically face several drawbacks. These include rapid switching in their control signals, sensitivity to noise, high control effort, and increased energy consumption. Adaptive control in EVs involves continuously monitoring various parameters such as battery charge level, motor temperature, and driving conditions, and adjusting the motor's control signals accordingly. In [18], a least mean square

adaptive control is proposed. It makes the engines run smoother and more evenly by keeping the motor's movements small and controlled, which helps prevent overheating and saves battery power. In [19], a two-layer fuzzy logic control system is proposed to enhance the sideways stability of hybrid electric vehicles. It determines the necessary yaw angle for stability and calculates the required braking force for the rear wheels to achieve that angle.

One of the common applications of adaptive control in EVs is the Adaptive Cruise Control (ACC). ACC-equipped vehicles use onboard sensors to understand the position and speed of surrounding vehicles and adjust the vehicle's driving patterns. This improves passenger comfort and battery energy utilization while ensuring safety [20]. The method in [21] improves cooperative ACC strategies for EVs by employing a hybrid optimization approach. The method considers the dynamic nature of traffic conditions and the need for energy-efficient driving. In [22], the control system optimized energy consumption by dynamically adjusting the vehicle's speed. This approach allows the ACC to predict and adapt to the vehicle's behaviour in real time.

ACCs use radar, cameras, or LiDAR to detect the distance and speed of leading vehicles. However, these sensors can face limitations in adverse weather conditions, leading to potential inaccuracies in the ACC system's decisions. ACCs often increase energy consumption due to more frequent acceleration and deceleration compared to human drivers, which can reduce the vehicle's range. Model Reference Adaptive Control (MRAC) is a control strategy designed to make a system follow the behaviour of a reference model. In [23], an adjustable reference model makes mode transitions smoother. The approach creates speed profiles, adjusts model settings with an online estimator, and uses MRAC to follow reference dynamics. In [24], the MRAC adjusts control parameters based on real-time inputs, to ensure smooth operation of the EV.

Most of existing adaptive control strategies such as MRAC assumes perfect agreement between the process model and the reference model, but real-world systems often have uncertainties such as parameter variations and non-linearity that can affect the performance of the adaptive control. In addition, designing MRAC systems involves the complex selection and tuning of adaptation laws, controller gains, and reference models, a process that tends to be complex and time-consuming. Achieving a delicate balance between rapid adaptation to changing conditions and stability against divergence is an additional challenge.

$\mathcal{L}1$ Adaptive Control (L1AC) offers a promising alternative for addressing several challenges associated with traditional control approaches. It mitigates issues such as chattering, sensitivity to noise, and high control effort in Sliding Mode Controls (SMCs); sensor limitations and increased energy consumption in Adaptive Cruise Control (ACC) systems; and the need for a perfect match between process and reference models, along with sensitivity to model uncertainty in Model Reference Adaptive Control (MRAC).

$\mathcal{L}$AC is a theory for the design of robust adaptive control architectures using fast adaptation schemes [25]. The key feature of $\mathcal{L}1$ adaptive control is the decoupling of the adaptation loop from the control loop, which allows arbitrarily fast adaptation without sacrificing robustness. This separation between adaptation and robustness

is achieved by explicitly building the robustness specification into the problem formulation. Fast adaptation allows compensation for the unwanted effects of rapidly changing uncertainties and significant changes in system dynamics. On the other hand, the bandwidth-limited filter keeps the robustness bounds away from zero in the presence of fast adaptation. The bandwidth and structure of this filter define the trade-off between performance and robustness of the closed-loop adaptive system [26].

In [27], $\mathcal{L}$AC is introduced to analyse the stability properties of its control signal, focusing on asymptotic stability. The authors then addressed the guaranteed transient performance of the controller, assessing its ability to provide stable and reliable responses during dynamic transitions [28]. In [29], an $\mathcal{L}$AC is designed for multirotor vehicle attitude control and provides an adaptive and robust solution for precise stabilisation. A safe feedback motion planning is proposed in [30], which combines contraction theory and $\mathcal{L}$AC for safe motion planning in dynamic systems. A comparative study in [31] evaluates the performance of $\mathcal{L}1$ adaptive controllers in different scenarios.

A robust $\mathcal{L}1$ fuzzy adaptive controller is introduced in [32] to improve the efficiency and stability of grid-connected photovoltaic systems. In [33], designing and modelling a quadcopter control system have been performed using $\mathcal{L}$AC. In [34], an $\mathcal{L}$AC is investigated in safety-critical systems, emphasising its robustness and adaptability for improved safety. In [35], the $\mathcal{L}$AC addresses control challenges in flexible spacecraft, improving stability in the presence of disturbances. In [36], $\mathcal{L}$AC for indoor autonomous vehicles is introduced aiming at flight testing. An innovative $\mathcal{L}$AC methodology for aerial refuelling is proposed in [37]. It emphasizes guaranteed transient performance in the dynamic and precise manoeuvres involved.

In this paper, the proposed robust control strategy includes a $\mathcal{L}1$ adaptive control to motion control of a simplified model of the EV. The model is first decomposed into two linear and nonlinear parts where the linear part is compensated using state feedback with a feedforward term. An adaptive methodology based on $\mathcal{L}1$ theory and low-pass filters are used to compensate the nonlinear part of the model. A projection algorithm is used to estimate the nonlinear parts of the EV dynamics. The proposed control algorithm features robustness again the model uncertainties, internally stable due to an auto tuned state feedback, ability to adjust the transient response and remove the effects of uncertainties.

This paper is organised as follows: Section II introduces the proposed control methodology for motion control of the electric vehicle. Section III describes the control-oriented dynamics of EV. Section IV includes the mathematical formulation of $\mathcal{L}1$ adaptive control. Section V provides the simulation results. Conclusion is drawn in Section VI.

2 Problem Statement

The central controller in EVs is responsible for delivering high performance by striking a balance between desired motion and acceleration capabilities. The control system for EVs must be robust and flexible to improve the static and dynamic performance of these systems. Adaptability in this context means the ability of the system to

adapt to vehicle operating parameters and changing road conditions. Fig. 1 outlines the proposed robust adaptive control strategy aimed at achieving the desired motion tracking in both transient and steady state conditions.

The key concept is to decompose the non-linear model of the vehicle into linear and non-linear components. To improve control effectiveness, a model reference dynamic is formulated to establish the desired performance pattern for the control system. The design incorporates a state feedback mechanism, complemented by a feedforward term, which is precisely designed to stabilise the internal linear dynamics and ensure minimal steady-state error. This approach is critical to maintaining the vehicle's performance in different operating states.

Incorporating $\mathcal{L}_1$ theory and Lyapunov stability, a nonlinear projection adaptation law is developed which allows the estimation of nonlinear parts of the EV even in the presence of uncertainties, thus contributing to the adaptability of the control system. The use of strictly monotonic filters improves the robustness of the control system to model uncertainties. According to Fig. 1, the control signal u is utilized in the state feedback mechanism along with a feedforward term to stabilize the internal linear dynamics of the EV. The desired longitude and lateral velocities alongside the desired yaw rate the target motion profile of the EV ($\mathbf{x}_r$). A model reference dynamic is formulated to define the desired performance pattern $\mathbf{x}_m$ for the control system. The state feedback mechanism is employed to both the EV and model reference dynamics. Using the error between the model reference and EV dynamics $\tilde{\mathbf{x}} = \mathbf{x}_m - \mathbf{x}$, the output of the projection adaptation law, denoted as $\Theta^T \tilde{\mathbf{x}}$, is responsible for instantaneously estimating the nonlinearities within the EV dynamics.

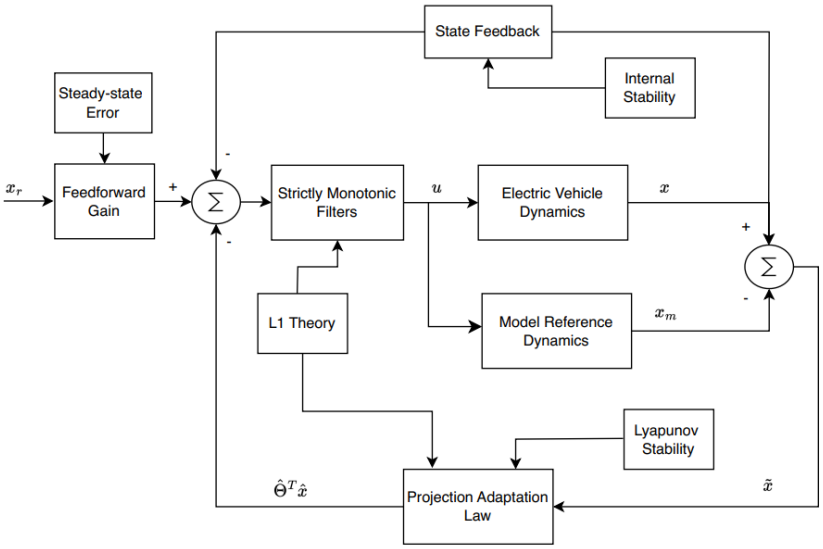

Fig. 1: Block diagram of the proposed robust adaptive control for the EV based on the model reference dynamics, and a projection-based adaptation law.

3 Control-Oriented EV Dynamics

In the context of planar motion, ground vehicles can be easily represented as rigid bodies with three degrees of freedom. These degrees of freedom are defined by three dynamic states: longitudinal velocity, lateral velocity and yaw rate. As observed in Fig. 2, the simplified motion equations for an EV in the plane x-y can be expressed as follows [38]:

$$\begin{aligned} m_v\left(\dot{v}_x - r v_y\right) &= F_x - C_a v_x^2 - C_r m_v g \\ m_v\left(\dot{v}_y + r v_x\right) &= F_y \\ I_z \dot{r} &= M_z \end{aligned} \tag{1}$$

where m_v represents the mass of the EV, and v_x, v_y, r, and I_z respectively denote the longitudinal velocity, lateral velocity, yaw rate, and the moment of inertia of the vehicle about the z-axis. The coordinates x, y, and z align with the vehicle's center of gravity. Generalized external forces acting along the x and y axes are denoted by F_x and F_y respectively. The generalized external torque about the z-axis is M_z. Additionally, C_d and C_r represent the coefficients of aerodynamic resistance and rolling resistance, while L_f and L_r signify the distances between the front and rear wheel axes, respectively.

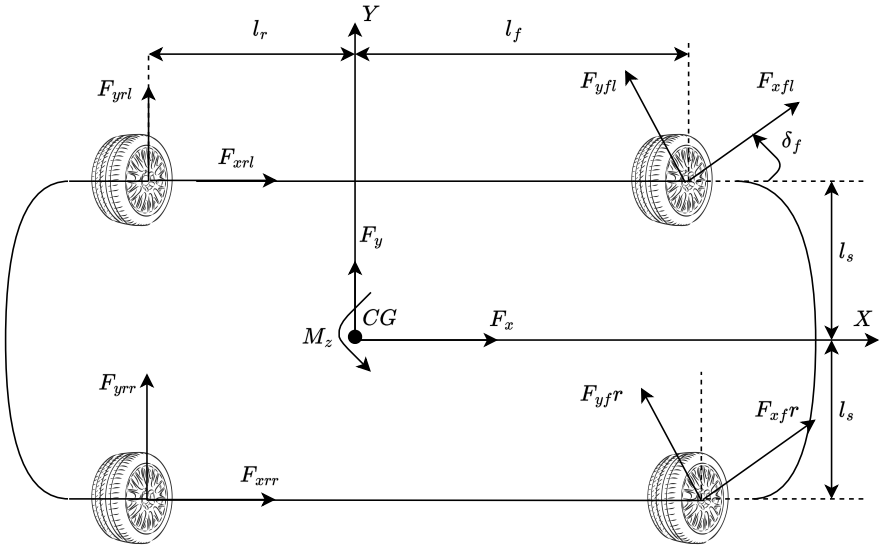

Fig. 2: Planar motion coordinates for Electric Ground Vehicles (EGV) [38].

Given that each of the four vehicle motors can be started or stopped independently, generalized forces or torques can be expressed as follows [38]:

$$\begin{aligned} F_X &= F_{xfl}\cos\delta_f - F_{yfl}\sin\delta_f + F_{xfr}\cos\delta_f - F_{yfr}\sin\delta_f + F_{xrl} + F_{xrr}, \\ F_Y &= F_{xfl}\sin\delta_f + F_{yfl}\cos\delta_f + F_{xfr}\sin\delta_f + F_{yfr}\cos\delta_f + F_{yrl} + F_{yrr}, \\ M_z &= l_s\left(-F_{xfl}\cos\delta_f + F_{yfl}\sin\delta_f + F_{xfr}\cos\delta_f - F_{yfr}\sin\delta_f + F_{xrr} - F_{xrl}\right) \\ &\quad + l_r\left(-F_{yrl} - F_{yrr}\right) + l_f\left(F_{xfl}\sin\delta_f + F_{yfl}\cos\delta_f + F_{xfr}\sin\delta_f + F_{yfr}\cos\delta_f\right) \end{aligned} \tag{2}$$

In the above equations, the steering angles of the left and right wheels at the front of the vehicle are considered nearly identical. They correspond to the steering angle of the vehicle δ scaled by the calibrated scaling rate β and can be expressed as $\delta_f = \alpha\delta$. The longitudinal force for each tire of the vehicle, independent of the tire model, can be expressed as follows using the rotational dynamics of each motor located in the wheels and the wheel pairs [38]:

$$J\dot{\omega}_i = T_i - F_{xi}R_{\text{eff}} \tag{3}$$

where J represents rotational inertia, and R denotes the effective radius of each wheel, assumed to be uniform. The index i identifies different motors located in the vehicle's wheels. The output torque of each motor T_i is positive during acceleration and negative during braking. Since the electrical response of a motor is much faster than the mechanical response, the dynamics between the control voltage signal and the motor output torque can be neglected. By defining state variables as $x_1 = v_x$, $x_2 = v_y$, and $x_3 = r$, the nonlinear dynamic model of the EV is given below:

$$\begin{aligned} \dot{x}_1 &= x_2x_3 - \frac{C_a}{m_v}x_1^2 - C_rg + \frac{1}{m_v}\left(-\frac{J}{R_{\text{eff}}}\Delta_{1x}\dot{\omega} - 2C_a\sin\delta_f\left(\delta_f - \frac{x_2 + l_fx_3}{x_1}\right)\right) + v_1 \\ \dot{x}_2 &= -x_1x_3 + \frac{1}{m_v}\left(-\frac{J}{R_{\text{eff}}}\Delta_{2x}\dot{\omega} + 2C_a\cos\delta_f\left(\delta_f - \frac{x_2 + l_fx_3}{x_1}\right) + 2C_a\frac{l_rx_3 - x_2}{x_1}\right) + v_2 \\ \dot{x}_3 &= \frac{1}{I_z}\left(-\frac{J}{R_{\text{eff}}}\Delta_{3x}\dot{\omega} + 2C_a\cos\delta_f\left(\delta_f - \frac{x_2 + l_fx_3}{x_1}\right) - 2C_a\frac{l_rx_3 - x_2}{x_1}\right) + v_3 \end{aligned} \tag{4}$$

where

$$\begin{aligned} \dot{\omega} &= \begin{bmatrix}\dot{\omega}_{fl} & \dot{\omega}_{fr} & \dot{\omega}_{rl} & \dot{\omega}_{rr}\end{bmatrix}^T \\ \Delta_{1x} &= \begin{bmatrix}\cos\delta_f & \cos\delta_f & 1 & 1\end{bmatrix}, \quad \Delta_{2x} = \begin{bmatrix}\sin\delta_f & \sin\delta_f & 0 & 0\end{bmatrix} \\ \Delta_{3x} &= \begin{bmatrix}l_f\sin\delta_f - l_s\cos\delta_f & l_s\sin\delta_f + l_f\cos\delta_f & l_s & l_s\end{bmatrix} \end{aligned} \tag{5}$$

Additionally, the virtual control v_d is defined as

$$\begin{aligned} v_d &= \begin{bmatrix}v_1 & v_2 & v_3\end{bmatrix}^T = Bu, \\ B &= \begin{bmatrix}\Delta_{1x}^T/m_vR_{\text{eff}} & \Delta_{2x}^T/m_vR_{\text{eff}} & \Delta_{3x}^T/I_zR_{\text{eff}}\end{bmatrix}^T \\ u &= \begin{bmatrix}u_1 & u_2 & u_3 & u_4\end{bmatrix}^T = \begin{bmatrix}T_{\text{fl}} & T_{\text{fr}} & T_{\text{rl}} & T_{\text{rr}}\end{bmatrix}^T \end{aligned} \tag{6}$$

It is assumed that the steering angles of the front and rear wheels are approximately equal and proportional to the vehicle's steering angle. Furthermore, the longitudinal force for each tire, independent of the tire model, can be expressed based on the rotational dynamics of the motors located at the wheel pairs as follows [38]:

$$J\dot{\omega}_i = T_i - F_{xi}R_{\text{eff}}, \quad i = fl, fr, rl, rr \tag{7}$$

The lateral tire frictional force is described through the tire model with the slip angles of the front and rear tires α_f and α_r respectively, and can be expressed as follows:

$$\begin{aligned} F_{yf} &= C_\alpha \alpha_f = C_\alpha \left(\delta_f - \frac{v_y + l_f r}{v_x} \right), \\ F_{yr} &= C_\alpha \alpha_r = C_\alpha \left(\frac{l_r r - v_y}{v_x} \right) \end{aligned} \tag{8}$$

Based on the vehicle kinematic model in [39], the linear speed of the wheels of the vehicle is equal to

$$\begin{aligned} v_{fl} &= (v_x + rl_s)\cos\delta_{fl} + (v_y + rl_f)\sin\delta_{fl}, \\ v_{fr} &= (v_x - rl_s)\cos\delta_{fr} + (v_y + rl_f)\sin\delta_{fr}, \\ v_{rl} &= v_x + rl_s, \\ v_{rr} &= v_x - rl_s. \end{aligned} \tag{9}$$

Then, the angular speed of each wheel during the vehicle manoeuvre can be expressed as follows [39]:

$$w_{fl} = \frac{v_{fl}}{R_{\text{eff}}}, w_{fr} = \frac{v_{fr}}{R_{\text{eff}}}, w_{rl} = \frac{v_{rl}}{R_{\text{eff}}}, w_{rr} = \frac{v_{rr}}{R_{\text{eff}}}. \tag{10}$$

The parameters of the dynamic model for the EVare presented in Table 1. The primary objective of the adaptive controller is initially to adapt the virtual controls v_d in equation (4) to guide the state variables x_1, x_2, and x_3 toward their desired values. Subsequently, these adapted controls are transformed into the actual control u in equation (6).

Table 1: The main parameters of the electric ground vehicle [38].

Parameter	**Description**	**Value**
m_v	Vehicle mass	800 Kg
I_z	Moment of inertia of the vehicle around the z axis.	729
C_a	Aerodynamic resistance coefficient	0.37
C_r	Rolling resistance coefficient	0.004
l_f	Longitudinal distance between the center and the rear wheels	0.85 m
l_r	Longitudinal distance between the center and the front wheels	1.04 m
l_s	Half of the vehicle track	0.7 m
δ_f	Wheel steering angle	$\pi/36$ rad
J	Rotational inertia of the wheel	$1.4\,\text{Kg}\cdot\text{m}^2$
g	Gravity acceleration	$9.8\,\text{m/s}^2$
R_{eff}	Effective radius of the wheel	0.312 m

4 Motion Control of EV using $\mathcal{L}_1$ Adaptive Control

The adaptive control strategy in this paper consists of a model reference model, a state feedback, feedforward gain and an adaptive control. The model reference is used to provide a desired dynamics pattern corresponding to desired motion profiles. In this section, first we extend a methodology based on the model reference adaptive control where the basic idea is to decompose the primary system dynamics into linear and nonlinear parts.

4.1 Model Reference Adaptive Control

Consider the nonlinear dynamics of the system presented as follows:

$$\begin{aligned} \dot{\mathbf{x}}(t) &= \mathbf{A}\mathbf{x}(t) + \mathbf{B}\mathbf{u}(t) + \mathbf{f}(t), \quad \mathbf{x}(0) = \mathbf{x}_0, \\ \mathbf{y}(t) &= \mathbf{C}^T\mathbf{x}(t). \end{aligned} \tag{11}$$

where $\mathbf{x} \in \mathbb{R}^n$ represents the system states, $\mathbf{A} \in \mathbb{R}^{n\times n}$ is the state matrix, $\mathbf{B} \in \mathbb{R}^{n\times m}$ and $\mathbf{C} \in \mathbb{R}^{r\times n}$ are input and output matrices, respectively. The nonlinear term $\mathbf{f} \in \mathbb{R}^n$ is an unknown state-dependent term that can be described as $\mathbf{f} = \mathbf{B}\boldsymbol{\theta}^T\mathbf{x}$, where $\boldsymbol{\theta} \in \mathbb{R}^{n\times m}$ is the matrix of unknown parameters. $\mathbf{u} \in \mathbb{R}^{m\times 1}$ is the control signal vector, and $\mathbf{y} \in \mathbb{R}^{r\times 1}$ is the output vector. The parameters n, m, and r denote the number of variable states, number of inputs, and number of outputs, respectively.

For a bounded continuous reference signal $\mathbf{y}_d \in \mathbb{R}^{r\times 1}$, the objective is to find an adaptive feedback control signal $\mathbf{u}(t)$ such that the output signal $\mathbf{y}(t)$ closely tracks the reference signal $\mathbf{y}_d$, while preserving boundedness and desired tracking characteristics. The desired control signal in the structure of the model reference control is directly formulated as follows:

$$\mathbf{u}_{mrac}(t) = -\mathbf{K}_m\mathbf{x} + \mathbf{K}_g\mathbf{r}(t) - \hat{\boldsymbol{\theta}}^T\mathbf{x}(t) \tag{12}$$

where $\hat{\boldsymbol{\theta}}$ is the estimation of $\boldsymbol{\theta}$. Considering $\mathbf{A}_m$ as the desired closed-loop matrix (stable matrix with desired eigenvalues), Equation (11) is rewritten as follows:

$$\begin{aligned} \dot{\mathbf{x}}(t) &= \mathbf{A}_m\mathbf{x}(t) + \mathbf{B}\left(\mathbf{u}(t) + \boldsymbol{\theta}^T\mathbf{x}(t)\right), \quad \mathbf{x}(0) = \mathbf{x}_0, \\ \mathbf{y}(t) &= \mathbf{C}^T\mathbf{x}(t), \end{aligned} \tag{13}$$

where $\mathbf{A}_m = \mathbf{A} - \mathbf{B}\mathbf{K}_m$. Corresponding to (12), the adaptive control law is given below:

$$\mathbf{u}_{ad}(t) = \mathbf{K}_g\mathbf{r}(t) - \hat{\boldsymbol{\theta}}^T\mathbf{x}(t) \tag{14}$$

The feedforward gain can be obtained as

$$\mathbf{K}_g = \left(\mathbf{C}^T\mathbf{A}_m^{-1}\mathbf{B}\right)^{-1} \tag{15}$$

The main goal of the control signal in (14) is to completely eliminate uncertainties in (13) and guide the system towards the desired reference system, formulated as follows:

$$\begin{aligned}\dot{\mathbf{x}}_m(t) &= \mathbf{A}_m\mathbf{x}(t) + \mathbf{B}\mathbf{K}_g\mathbf{r}(t), \quad \mathbf{x}_m(0) = \mathbf{x}_0,\\ \mathbf{y}_m(t) &= \mathbf{C}^T\mathbf{x}_m(t)\end{aligned} \tag{16}$$

By substituting (14) into (16), the closed-loop dynamics will be equal to:

$$\begin{aligned}\dot{\mathbf{x}}(t) &= \left(\mathbf{A}_m - \mathbf{B}\hat{\boldsymbol{\theta}}^T(t)\right)\mathbf{x}(t) + \mathbf{B}\mathbf{K}_g\mathbf{r}(t), \quad \mathbf{x}(0) = \mathbf{x}_0,\\ \mathbf{y}(t) &= \mathbf{C}^T\mathbf{x}(t),\end{aligned} \tag{17}$$

where $\tilde{\boldsymbol{\theta}}(t) \triangleq \hat{\boldsymbol{\theta}}(t) - \boldsymbol{\theta}$ represents the vector of parameter estimation error. By defining the tracking error signal as $\mathbf{e}(t) \triangleq \mathbf{x}_m(t) - \mathbf{x}(t)$, the tracking error dynamics will be:

$$\dot{\mathbf{e}}(t) = \mathbf{A}_m\mathbf{e}(t) + \mathbf{B}\tilde{\boldsymbol{\theta}}^T(t)\mathbf{x}(t), \quad \mathbf{e}(0) = 0, \tag{18}$$

The parameter adaptation law in direct model reference adaptive control is given by:

$$\dot{\hat{\boldsymbol{\theta}}}(t) = -\boldsymbol{\eta}\mathbf{x}(t)\mathbf{e}^T(t)\mathbf{P}\mathbf{B}, \quad \hat{\boldsymbol{\theta}}(0) = \hat{\boldsymbol{\theta}}_0, \tag{19}$$

where η is the adaptation gain. The positive definite matrix $\mathbf{P} = \mathbf{P}^T > 0$ is obtained by solving the following matrix algebraic equation:

$$\mathbf{A}_m^T\mathbf{P} + \mathbf{P}\mathbf{A}_m = -\mathbf{Q} \tag{20}$$

where $\mathbf{Q} = \mathbf{Q}^T > 0$ is an arbitrary positive definite matrix. The adaptation law presented in equation (19) is determined based on the stability of the closed-loop system using the Lyapunov method. In other words, consider the Lyapunov function as follows:

=

$$v\left(\mathbf{e}(t), \hat{\boldsymbol{\theta}}(t)\right) = \mathbf{e}^T(t)\mathbf{P}\mathbf{e}(t) + \frac{1}{\eta}\sum_{i=1}^{m}\tilde{\boldsymbol{\theta}}_i^T(t)\tilde{\boldsymbol{\theta}}_i(t) \tag{21}$$

where $\tilde{\boldsymbol{\theta}} = [\tilde{\boldsymbol{\theta}}_{\mathbf{1}}, \tilde{\boldsymbol{\theta}}_{\mathbf{2}}, ..., \tilde{\boldsymbol{\theta}}_{\boldsymbol{m}}]$. The next step is to examine the time derivative of the Lyapunov function given by (21):

$$\frac{dv\left(\mathbf{e}(t), \hat{\boldsymbol{\theta}}(t)\right)}{dt} = \dot{\mathbf{e}}^T(t)\mathbf{P}\mathbf{e}(t) + \mathbf{e}^T(t)\mathbf{P}\dot{\mathbf{e}}(t) + \frac{2}{\eta}\sum_{i=1}^{m}\tilde{\boldsymbol{\theta}}_i^T(t)\dot{\tilde{\boldsymbol{\theta}}}_i(t) \tag{22}$$

By substituting the relation (18) into equation (22), we have:

$$\begin{aligned}\dot{v} = {} & \mathbf{e}^T(t)\mathbf{A}_m^T\mathbf{P}\mathbf{e}(t) + \mathbf{x}^T(t)\tilde{\boldsymbol{\theta}}(t)\mathbf{B}^T\mathbf{P}\mathbf{e}(t)\\ & + \mathbf{e}^T(t)\mathbf{P}\mathbf{A}_m\mathbf{e}(t) + \mathbf{e}^T(t)\mathbf{P}\mathbf{B}\tilde{\boldsymbol{\theta}}^T(t)\mathbf{x}(t) + \frac{2}{\eta}\sum_{i=1}^{m}\tilde{\boldsymbol{\theta}}_i^T(t)\dot{\tilde{\boldsymbol{\theta}}}_i(t)\end{aligned} \tag{23}$$

Considering the following relations:

$$\begin{cases}\mathbf{x}^T(t)\tilde{\boldsymbol{\theta}}(t)\mathbf{B}^T\mathbf{P}\mathbf{e}(t) \in \mathbb{R} \rightarrow (\mathbf{x}^T(t)\tilde{\boldsymbol{\theta}}(t)\mathbf{B}^T\mathbf{P}\mathbf{e}(t)) = (\mathbf{x}^T(t)\tilde{\boldsymbol{\theta}}(t)\mathbf{B}^T\mathbf{P}\mathbf{e}(t))^T \\ \mathbf{e}^T(t)\mathbf{P}\mathbf{B}\tilde{\boldsymbol{\theta}}^T(t)\mathbf{x}(t) = (\mathbf{e}^T(t)\mathbf{P}\mathbf{B}\tilde{\boldsymbol{\theta}}^T(t)\mathbf{x}(t))^T\end{cases}$$

The time derivative of the Lyapunov function in (23) is

$$\frac{dv\left(\mathbf{e}(t), \hat{\boldsymbol{\theta}}(t)\right)}{dt} = \mathbf{e}^T(t)(\mathbf{A}_m^T\mathbf{P} + \mathbf{P}\mathbf{A}_m)\mathbf{e}(t) + \left(2\sum_{i=1}^{m}\frac{1}{\eta}\tilde{\boldsymbol{\theta}}_i^T(t)\dot{\tilde{\boldsymbol{\theta}}}_i(t) + a_i\tilde{\boldsymbol{\theta}}_i^T\mathbf{x}\right) \tag{24}$$

where $\mathbf{a} = \mathbf{e}^T\mathbf{P}\mathbf{B} = [a_1, a_2, ..., a_m]$ By substituting (20) into (24), the Lyapunov function derivative will be:

$$\frac{dv\left(\mathbf{e}(t), \hat{\boldsymbol{\theta}}(t)\right)}{dt} = -\mathbf{e}^T(t)\mathbf{Q}\mathbf{e}(t) + 2\dot{\tilde{\boldsymbol{\theta}}}^T(t)\left(2\sum_{i=1}^{m}\frac{1}{\eta}\tilde{\boldsymbol{\theta}}_i^T(t)\dot{\tilde{\boldsymbol{\theta}}}_i(t) + a_i\tilde{\boldsymbol{\theta}}_i^T\mathbf{x}\right) \tag{25}$$

To ensure that the time derivative of the Lyapunov function to remain consistently negative, the term inside the parentheses in (25) must be equal to zero. In other words:

$$\sum_{i=1}^{m}\frac{1}{\eta}\tilde{\boldsymbol{\theta}}_i^T(t)\dot{\tilde{\boldsymbol{\theta}}}_i(t) + a_i\tilde{\boldsymbol{\theta}}_i^T\mathbf{x} = 0 \rightarrow \frac{dv\left(\mathbf{e}(t), \hat{\boldsymbol{\theta}}(t)\right)}{dt} = -\mathbf{e}^T(t)\mathbf{Q}\mathbf{e}(t) \leq 0 \tag{26}$$

Therefore, if the following relation holds, the time derivative of the Lyapunov function will always be negative, and the closed-loop system will be asymptotically stable:

$$\begin{gathered}\sum_{i=1}^{m}\frac{1}{\eta}\tilde{\boldsymbol{\theta}}_i^T(t)\dot{\tilde{\boldsymbol{\theta}}}_i(t) + a_i\tilde{\boldsymbol{\theta}}_i^T\mathbf{x} = 0 \rightarrow \dot{\tilde{\theta}}_i = -\eta a_i\mathbf{x}(t) \rightarrow \dot{\tilde{\theta}} = -\eta\mathbf{x}\mathbf{e}^T\mathbf{P}\mathbf{B} \\ \rightarrow (\dot{\hat{\boldsymbol{\theta}}} - \dot{\boldsymbol{\theta}}) = -\eta\mathbf{x}\mathbf{e}^T\mathbf{P}\mathbf{B} \rightarrow \dot{\hat{\theta}} = -\eta\mathbf{x}\mathbf{e}^T\mathbf{P}\mathbf{B}\end{gathered} \tag{27}$$

Given the above relations, under the adaptation law in (27), the error signals $\mathbf{e}(t)$, $\hat{\theta}(t)$ will remain bounded. Since $\mathbf{x}(t) = \mathbf{x}_m(t) - \mathbf{e}(t)$ and $\mathbf{x}_m(t)$ represent stable model states, the boundedness of $\mathbf{e}(t)$ corresponds to the boundedness of the main system states. To investigate whether the tracking error ultimately converges to zero, we take the second-time derivative of the Lyapunov function.

$$\dot{v}(t) = -\mathbf{e}^T(t)\mathbf{Q}\mathbf{e}(t) \tag{28}$$

Given that $\dot{\mathbf{e}}(t)$ is a bounded signal, the second-time derivative of the Lyapunov function is also bounded, and its first derivative is continuously uniform.

4.2 $\mathcal{L}1$ Adaptive Control

Considering the system dynamics described in (11), the $\mathcal{L}_1$ control law is given below:

$$\mathbf{u}(t) = \mathbf{u}_m(t) + \mathbf{u}_{ad}(t), \quad \mathbf{u}_m(t) = -\mathbf{K}_m \mathbf{x}^T(t) \tag{29}$$

By substituting (29) into (13), the closed-loop system dynamics transforms as follows:

$$\begin{aligned} \dot{\mathbf{x}}(t) &= \mathbf{A}_m \mathbf{x}(t) + \mathbf{B}(\boldsymbol{\theta}^T \mathbf{x}(t) + \mathbf{u}_{ad}(t)), \quad \mathbf{x}(0) = \mathbf{x}_0 \\ \mathbf{y}(t) &= \mathbf{C}\mathbf{x}(t) \end{aligned} \tag{30}$$

where $\boldsymbol{\theta}$ is the unknown parameter matrix. Consider the following model reference dynamics:

$$\begin{aligned} \dot{\mathbf{x}}_m(t) &= \mathbf{A}_m \mathbf{x}_m(t) + \mathbf{B}\mathbf{K}_g \mathbf{r}(t), \quad \mathbf{x}_m(0) = \mathbf{x}_0 \\ \mathbf{y}_m(t) &= \mathbf{C}\mathbf{x}_m(t) \end{aligned} \tag{31}$$

To estimate the nonlinear parts of EV dynamics, the projection adaptation law is given by:

$$\dot{\hat{\boldsymbol{\theta}}}(t) = \eta \text{Proj}(\hat{\boldsymbol{\theta}}(t), -\mathbf{x}(t)\mathbf{e}^T(t)\mathbf{P}\mathbf{B}), \quad \hat{\boldsymbol{\theta}}(0) = \hat{\boldsymbol{\theta}}_0 \tag{32}$$

where $\dot{\tilde{\boldsymbol{x}}}(t) = \mathbf{x}_m(t) - \mathbf{x}(t)$ is the prediction error, and the adaptation gain is $\boldsymbol{\eta}$. The matrix $\mathbf{P} = \mathbf{P}^T > 0$ is determined by solving the algebraic equation $\mathbf{A}_m^T \mathbf{P} + \mathbf{P}\mathbf{A}_m = -\mathbf{Q}$, and for any positive definite symmetric matrix $\mathbf{Q}$. Consider a closed convex set with a smooth boundary as follows:

$$\Omega_c = \{\boldsymbol{\theta} \in \mathbb{R}^n | f(\boldsymbol{\theta}) \leq c\}, \quad 0 \leq c \leq 1, \tag{33}$$

where $f(\boldsymbol{\theta})$ the convex uniformly continuous function is defined as follows:

$$f(\boldsymbol{\theta}) = \frac{(\epsilon_\theta + 1)\boldsymbol{\theta}^T \boldsymbol{\theta} - \theta_{\max}^2}{\epsilon_\theta \theta_{\max}^2} \tag{34}$$

where $\theta_{\max}$ is the upper bound of $\boldsymbol{\theta}$, and ϵ_θ is a positive-valued threshold. The projection operator is defined as follows:

$$\text{Proj}(\boldsymbol{\theta}, \mathbf{y}) = \begin{cases} \mathbf{y} & \text{if } f(\boldsymbol{\theta}) < 0 \text{ or } (f(\boldsymbol{\theta}) \geq 0 \text{ and } \nabla f^T \mathbf{y} \leq 0) \\ \mathbf{y} - \frac{\nabla f}{\|\nabla f\|^2} \nabla f^T \mathbf{y} & \text{if } f(\boldsymbol{\theta}) \geq 0 \text{ and } \nabla f^T \mathbf{y} > 0, \end{cases} \tag{35}$$

According to (35), the projection operator will not change the value of $\mathbf{y}$ as long as $\boldsymbol{\theta}$ belongs to the set $\Omega_0 = \{\boldsymbol{\theta} \in \mathbb{R}^n | f(\boldsymbol{\theta}) \leq 0\}$. However, if $f(\boldsymbol{\theta})$ is positive, the change in $\boldsymbol{\theta}$ depends on the sign of $\nabla f^T \mathbf{y}$. If $\nabla f^T \mathbf{y}$ is positive, the projection operator shrinks the vector $\mathbf{y}$ proportional to a vector normal to the boundary of the set $\Omega_{f(\mathbf{y})} = \{\boldsymbol{\theta} \in \mathbb{R}^n | f(\boldsymbol{\theta}) = f(\mathbf{y})\}$. This process transforms the uniform vector $\mathbf{y}$ into a tangent vector in the vector field $\Omega_1 = \{\boldsymbol{\theta} \in \mathbb{R}^n | f(\boldsymbol{\theta}) \leq 1\}$. The adaptive control law $\mathbf{u}_{ad}(t)$ in Laplace transform form is defined as follows:

$$\mathbf{U}_{ad}(s) = -\mathbf{C}(s)(\boldsymbol{\mu}(s) - \mathbf{K}_g \mathbf{R}(s)) \tag{36}$$

where $\mathbf{R}(s)$ and $\boldsymbol{\mu}(s)$ represent the Laplace transforms of $r(t)$ and $\hat{\boldsymbol{\theta}}^T\mathbf{x}(t)$, respectively. The feedforward gain is given by $\mathbf{K}_g = -(\mathbf{C}^T\mathbf{A}_m^{-1}\mathbf{B})^{-1}$, and $\mathbf{C}(s)$ is a strictly proper and stable filter with a DC gain of zero. This filter is to enhance the closed-loop robustness.

4.3 $\mathcal{L}1$ Adaptive Control Transient and Steady State Analysis

Consider the non-adaptive system for the closed-loop reference system below:

$$\begin{aligned}
&\dot{\mathbf{x}}_{ref}(t) = \mathbf{A}\mathbf{x}_{ref}(t) + \mathbf{B}(\boldsymbol{\theta}^T\mathbf{x}_{ref}(t) + \mathbf{u}_{ref}(t)), \quad \mathbf{x}_{ref}(0) = \mathbf{x}_0,\\
&\mathbf{u}_{ref}(s) = -\mathbf{C}(s)(\boldsymbol{\theta}^T\mathbf{x}_{ref}(s) - \mathbf{K}_g\mathbf{R}(s)) - \mathbf{K}_m^T\mathbf{x}_{ref}(s),\\
&\mathbf{y}_{ref}(s) = \mathbf{C}\mathbf{x}_{ref}(s).
\end{aligned} \tag{37}$$

The $\mathcal{L}1$ adaptive controller structure in (37) aims to compensate for the uncertainties of the system within the bandwidth of $\mathbf{C}(s)$.

Lemma 1: If $\|\mathbf{G}(s)\|_{L_1} < 1/L$ is true, then the system presented in (37) is stable and has bounded-input, bounded-output properties with respect to $r(t)$ and $\mathbf{x}_0$ [25].

Now consider the following dynamics:

$$\dot{\tilde{\mathbf{x}}}(t) = \mathbf{A}_m\tilde{\mathbf{x}}(t) + \mathbf{B}(\tilde{\boldsymbol{\theta}(t)}\mathbf{x}(t)), \quad \tilde{\mathbf{x}}(0) = 0 \tag{38}$$

where $\dot{\boldsymbol{\theta}}(t) = \boldsymbol{\theta}(t) - \boldsymbol{\theta}$.

Lemma 2: The prediction error in (38) is uniformly bounded. In other words,

$$|\boldsymbol{x}|\infty \leq \sqrt{\frac{\theta\max}{\lambda_{\min}(\boldsymbol{P})}\eta}, \quad \theta_{\max} = 4\max|\boldsymbol{\theta}|^2 \tag{39}$$

where $\lambda_{\min}(\boldsymbol{P})$ is the smallest eigenvalue of the matrix $\boldsymbol{P}$.

Proof: Consider the following Lyapunov function:

$$\boldsymbol{V}(\hat{\boldsymbol{x}}(t), \boldsymbol{\theta}) = \hat{\boldsymbol{x}}^T(t)\boldsymbol{P}\hat{\boldsymbol{x}}(t) + \frac{1}{\eta}\boldsymbol{\theta}^T(\boldsymbol{\theta}(t) - \boldsymbol{\theta}) \tag{40}$$

Using the projection adaptation law in (32), the time derivative of (40) will be equal to:

$$\begin{aligned}
\dot{\boldsymbol{V}}(t) &= \hat{\boldsymbol{x}}^T(t)\boldsymbol{P}\boldsymbol{x}(t) + \hat{\boldsymbol{x}}^T(t)\boldsymbol{P}\boldsymbol{x}(t) +\\
&\quad \frac{1}{\eta}\left(\boldsymbol{\theta}^T(\boldsymbol{A}\mathrm{m}^T + \boldsymbol{P}\boldsymbol{A}\mathrm{m})\boldsymbol{x}(t) + 2\hat{\boldsymbol{x}}^T(t)\boldsymbol{P}\boldsymbol{B}\boldsymbol{\theta}^T(t)\boldsymbol{x}(t) + 2\boldsymbol{\theta}^T(\boldsymbol{\theta}(t) - \boldsymbol{\theta})\right)\\
&= -\hat{\boldsymbol{x}}^T(t)\boldsymbol{Q}\boldsymbol{x}(t) + 2\hat{\boldsymbol{x}}^T(t)\boldsymbol{P}\boldsymbol{B}\boldsymbol{\theta}^T(t)\boldsymbol{x}(t)\\
&+2\boldsymbol{\theta}^T(\boldsymbol{\theta}(t) - \boldsymbol{\theta})\mathrm{Proj}(\boldsymbol{\theta}(t) - \boldsymbol{x}(t)\hat{\boldsymbol{x}}^T(t)\boldsymbol{P}\boldsymbol{B})\\
&\leq -\hat{\boldsymbol{x}}^T(t)\boldsymbol{Q}\boldsymbol{x}(t) + 2\boldsymbol{\theta}^T(t)\left(\boldsymbol{x}(t)\hat{\boldsymbol{x}}^T(t)\boldsymbol{P}\boldsymbol{B} + \mathrm{Proj}(\boldsymbol{\theta}(t) - \boldsymbol{x}(t)\hat{\boldsymbol{x}}^T(t)\boldsymbol{P}\boldsymbol{B})\right)\\
&\leq -\hat{\boldsymbol{x}}^T(t)\boldsymbol{Q}\boldsymbol{x}(t)
\end{aligned} \tag{41}$$

Assuming $\hat{\boldsymbol{x}}(0) = 0$, we can write

$$\lambda_{\min}(\boldsymbol{P})|\hat{\boldsymbol{x}}(t)|^2 \leq \boldsymbol{V}(t) \leq \boldsymbol{V}(0) = \frac{\boldsymbol{\theta}^T(0)\boldsymbol{\theta}(0)}{\eta} \tag{42}$$

Therefore, the projection law ensures that $\boldsymbol{\theta}$ remains inside a closed convex set, which means that

$$\frac{\boldsymbol{\theta}^T(0)\boldsymbol{\theta}(0)}{\eta} \leq \frac{4\max|\boldsymbol{\theta}|^2}{\eta} \tag{43}$$

The above relation implies that the tracking error is bounded. In other words,

$$|\boldsymbol{x}(t)| \leq \frac{\theta_{\max}}{\lambda_{\min}(\boldsymbol{P})\eta} \tag{44}$$

Using the control law in (29) and condition presented in Lemma 1, the tracking error asymptotically converge to zero, i.e. $\lim_{t\to\infty} \boldsymbol{x}(t) = 0$ [25].

The robustness of the proposed algorithm relies on the adaptation laws, which are tasked with estimating the nonlinearities in EV dynamics. To validate this robustness, it is sufficient to demonstrate that these adaptation laws converge to the optimal estimations. Using Lyapunov theory, we established the convergence of the adaptation laws through equations (21) and (28). There were no specific assumptions or limitations imposed in determining the adaptation law. The convergence and stability of the projection-based adaptation law described in equation (32) have been rigorously proved and discussed in Section 4.3.

5 Simulation Results and Discussion

The basis of the proposed adaptive control in this research is to separate the nonlinear dynamic model of the system under control into linear and nonlinear parts. To achieve this, the angular velocity dynamics of the vehicle's wheels must first be rewritten in terms of state variables. According to (9) and (10), the derivative of the wheels' angular velocities is given by:

$$\dot{\omega}_{\text{fl}} = \frac{\dot{x}_1\cos\delta_f + \dot{x}_3(l_f\sin\delta_f + l_s\cos\delta_f)}{R_{\text{eff}}}, \qquad \dot{\omega}_{\text{rl}} = \frac{(\dot{x}_1 + l_s\dot{x}_3)}{R_{\text{eff}}}, \tag{45}$$

$$\dot{\omega}_{\text{fr}} = \frac{\dot{x}_1\cos\delta_f + \dot{x}_3(l_f\sin\delta_f - l_s\cos\delta_f)}{R_{\text{eff}}}, \qquad \dot{\omega}_{\text{rr}} = \frac{(\dot{x}_1 + l_s\dot{x}_3)}{R_{\text{eff}}} \tag{46}$$

It's assumed that the product of vehicle lateral speed and front wheel steering angle is negligible. The nonlinear dynamic model of an EV can be described using the following parametric coefficients:

$$\begin{aligned}
\dot{x}_1 &= x_2x_3 + \alpha_1x_1^2 + \alpha_2 + \alpha_3\Delta_{1x}\dot{\omega} + \alpha_4 f_a(\boldsymbol{x}) + v_1\\
\dot{x}_2 &= -x_1x_3 + \beta_1\Delta_{2x}\dot{\omega} + \beta_2 f_a(\boldsymbol{x}) + \beta_3 f_b(\boldsymbol{x}) + v_2\\
\dot{x}_3 &= \gamma_1\Delta_{1x}\dot{\omega} + \gamma_2 f_a(\boldsymbol{x}) + \gamma_3 f_b(\boldsymbol{x}) + v_3
\end{aligned} \tag{47}$$

where

$$\alpha_1 = \frac{-C_a}{m}, \quad \alpha_2 = -C_r g, \quad \alpha_3 = -\frac{J}{m_v R_{\text{eff}}}, \quad \alpha_4 = -\frac{2C_a \sin\delta_f}{m_v},$$
$$\beta_1 = \frac{J}{m_v R_{\text{eff}}}, \quad \beta_2 = -\frac{2C_a \cos\delta_f}{m_v}, \quad \beta_3 = \frac{2C_a}{m_v},$$
$$\gamma_1 = -\frac{J}{I_z R_{\text{eff}}}, \quad \gamma_2 = \frac{2C_a \cos\delta_f}{I_z}, \quad \gamma_3 = \frac{-2C_a}{I_z},$$
$$f_a(\boldsymbol{x}) = \delta_f - \frac{x_2 + L_f x_3}{x_1}, \quad f_b(\boldsymbol{x}) = -\frac{L_r x_3 - x_2}{x_1}$$

Equation (46) can be described in the following quasi-linear state-space form dependent on the state:

$$\dot{\boldsymbol{x}} = \boldsymbol{A}(\boldsymbol{x})\boldsymbol{x} + \boldsymbol{B}\boldsymbol{v} + \boldsymbol{f}(\boldsymbol{x}) \tag{48}$$

where

$$\boldsymbol{A}(\boldsymbol{x}) = \begin{bmatrix} h_{11}x_1 & h_{12}x_3 & h_{13}x_2 \\ h_{21}x_1 & h_{22}x_3 & h_{23}x_2 \\ h_{31}x_1 & h_{32}x_3 & h_{33}x_2 \end{bmatrix}, \boldsymbol{B} = \begin{bmatrix} g_{11} & g_{12} & 0 \\ g_{21} & g_{22} & 0 \\ g_{31} & g_{32} & 1 \end{bmatrix}, \boldsymbol{f}(\boldsymbol{x}) = \begin{bmatrix} h_{14} & h_{15} & f_a(\boldsymbol{x}) \\ h_{24} & h_{25} & f_b(\boldsymbol{x}) \\ h_{34} & h_{35} & f_{g3} \end{bmatrix}$$

with the coefficients

$$h_{11} = -\frac{\alpha_1 - \alpha_2\alpha_3\beta_1}{d_a}, \quad h_{12} = -\frac{\alpha_1\alpha_3}{d_a}, \quad h_{13} = \frac{\alpha_3\alpha_4}{d_a},$$
$$h_{14} = \frac{\alpha_1 + \alpha_2\alpha_3\beta_1}{d_a}, \quad h_{15} = -\frac{\alpha_1\alpha_3}{d_a}, \quad h_{21} = -\frac{1 + \alpha_1\alpha_3}{d_a},$$
$$h_{22} = \frac{\beta_2 - \alpha_1\alpha_3\beta_2}{d_a}, \quad h_{23} = h_{21}, \quad h_{24} = h_{21}, \quad h_{25} = h_{22}.$$
$$h_{31} = \gamma_1\alpha_1 + \gamma_2, \quad h_{32} = \gamma_1\beta_1 + \gamma_2, \quad h_{33} = \gamma_1\beta_2,$$
$$h_{34} = \gamma_1 + \gamma_2, \quad h_{35} = \gamma_1 + \gamma_3,$$
$$g_{11} = -\frac{\alpha_1}{d_a}, \quad g_{12} = -\frac{\alpha_1}{d_a}, \quad g_{21} = g_{11}, \quad g_{22} = -\frac{\alpha_3\beta_1}{d_a},$$
$$g_{31} = \gamma_1(g_{11} + g_{21}), \quad g_{32} = \gamma_1(g_{21} + g_{31}), \quad g_{33} = \gamma_1(g_{11} + g_{31}),$$
$$f_{g1} = -\frac{\alpha_1\alpha_2\beta_1}{d_a}, \quad f_{g2} = \frac{\alpha_2\alpha_4\beta_1}{d_a}, \quad f_{g3} = \frac{\alpha_1}{d_a}.$$

The primary EV dynamics are initially presented in equations (1), (2), and (3), which are not expressed in state-space form. These equations are integrated into a state-space model because the proposed L1 adaptive control strategy, along with its relevant analysis and the procedure for deriving the adaptation laws, relies on a vector-matrix state-space representation of the EV dynamics.

By converting the vehicle dynamics into a state-space model, we can more effectively apply the L1 adaptive control strategy, which is designed to work within a

state-space framework. This approach allows for a detailed and precise formulation of the control strategy, taking into account the specific dynamic characteristics of the vehicle. The state-space model enables us to efficiently prove the internal stability, obtain the minimum steady-state error using a feedforward gain and particularly determine an explicit form for adaptation laws.

In this section, two different manoeuvres are conducted to validate the proposed L1 Adaptive control design using simulation results. The performance in terms of EV planar motion tracking, torque distribution, and power consumption is compared with the conventional Model Reference Adaptive Control (MRAC) and the Super Twisting Sliding Mode Control (STSMC) proposed in [35]. The first reference model for the vehicle planer motion tracking control is given below:

$$
\begin{aligned}
v_{xr} &= \begin{cases} 0.4667t + 5.6, & \text{if } t \leq 6 \\ 8.4, & \text{otherwise} \end{cases}, \\
v_{yr} &= \begin{cases} 0.01, & \text{if } t \leq 10 \\ 0.01 + 0.035(t-10), & \text{if } 10 < t \leq 14 \\ 0.15, & \text{otherwise} \end{cases}, \\
r_r &= \begin{cases} 0.01, & \text{if } t \leq 10 \\ 0.01 + 0.03(t-10), & \text{if } 10 < t \leq 14 \\ 0.13, & \text{otherwise} \end{cases}
\end{aligned}
\tag{49}
$$

This paper focuses on low speed manoeuvres as we wanted to address the robustness of the proposed approach. The desired longitudinal speed ranges from 5 m/sec to about 8.5 m/sec, corresponding to about 18 km/h to 31.7 km/h (or about 11.2 mph to 19.7 mph). The lateral speed ranges from 0 to 0.15 rad/sec. These speeds are appropriate for typical urban driving or low speed manoeuvring. This range indicates a maximum lateral speed of approximately 0.15 rad/sec, which equates to approximately 8.6 degrees per second. This is reasonable for typical low speed cornering and manoeuvring. A yaw rate of 0.12 rad/sec is approximately 6.9 degrees per second. This range is suitable for moderate steering manoeuvres.

The sampling time and simulation time are set to 0.001 and 20 seconds, respectively. The adaptation gain is set to 0.01, and the desired poles of the reference model are set to -5. All simulations were conducted using Simulink in MATLAB. Figure 3 shows the control algorithm simulated in Simulink.

According to Fig. 4, the velocity gradually increases from zero towards the desired velocity, following a typical S-shaped curve indicative of controlled systems. Lateral velocities remain relatively small throughout the observed period. The yaw rate initially accelerates from zero, overshoots the desired rate, and then stabilizes to the desired constant value. Three virtual control signals exhibit distinct behaviours: one decreases sharply, another rises rapidly before stabilizing, and the third settles to a constant positive value after an initial spike.

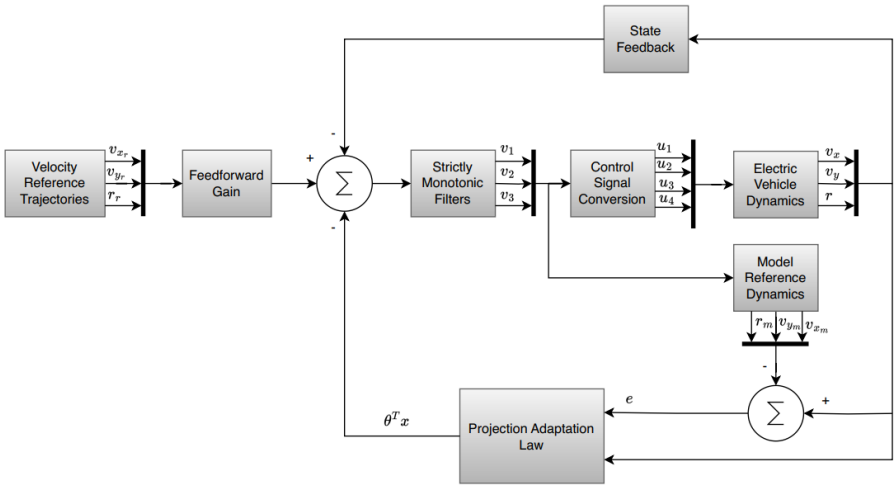

Fig. 3: Proposed control algorithm simulated in Simulink of MATLAB.

Fig. 5 illustrates the dynamic behaviour of torque outputs applied to individual wheels of the vehicle. During the first 6 seconds, the torque signals start at approximately 70 N.m and gradually decrease to around 15 N.m. Between 6 and 10 seconds, these torque signals further reduce to about 2 N.m. Throughout this 10-second period, the longitudinal velocity gradually increases, while the lateral velocity and yaw rate remain at zero. As the longitudinal velocity stabilizes and both the lateral velocity and yaw rate begin to increase, the torques applied to the forward and rear wheels on the left side gradually decrease to around zero. In contrast, the torques for the forward and rear wheels on the rightside increase and converge to approximately 1 N.m.

The results illustrate the correlation between torque signals and vehicle kinematics, highlighting how torque adjustments are utilized to control the vehicle's motion. The initial reduction in torque corresponds to the phase where the vehicle is accelerating in the longitudinal direction. As the vehicle transitions to a state where lateral velocity and yaw rate are introduced, torque redistribution occurs to maintain stability and achieve the desired trajectory. The reduction in left-side torques coupled with the increase in right-side torques suggests a coordinated control strategy to manage the vehicle's directional changes effectively. This dynamic adjustment of torques is crucial for precise vehicle handling and stability during different phases of motion.

The torque signals are obtained through a simulation program, where there are no physical constraints. As a result, the control system can increase the torque from zero to approximately 60 N·m in less than 0.01 seconds. However, in practice, such rapid torque changes would be constrained by physical limitations, power electronics capabilities, motor design, and battery constraints. Therefore, in real-world applications, torque changes must be much smoother to account for these limitations and ensure reliable and safe operation. This fast transient behaviour observed in the simulation is not a drawback of the proposed algorithm; rather, it is a result of the ideal conditions

provided by the simulation environment. The algorithm's performance in real-world scenarios will be adjusted to accommodate practical constraints while still benefiting from the robustness and effectiveness demonstrated in the simulation.

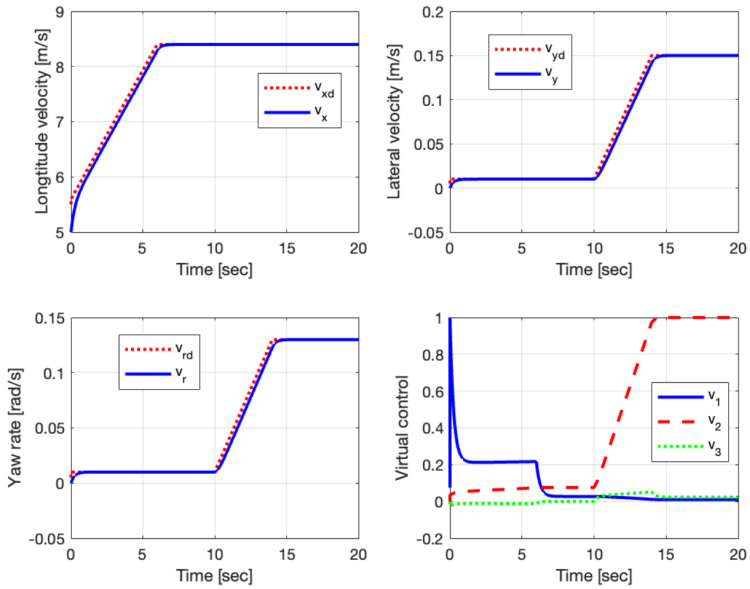

Fig. 4: Motion Tracking control outcomes and virtual control signals.

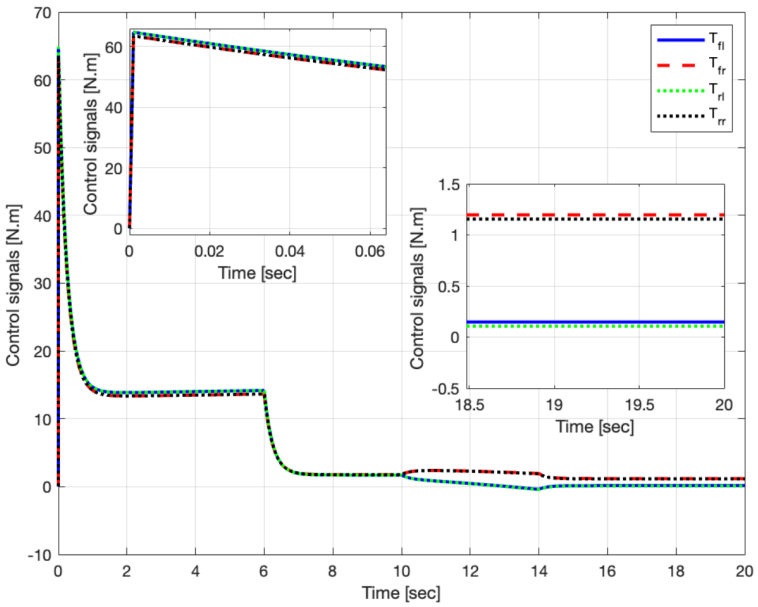

Fig. 5: Torque signals during the first maneuver of the EV using the proposed method.

Fig. 6 demonstrate the performance of the projection algorithm in estimating three nonlinear components of the electric vehicle's dynamics over a 20-second period. The true and estimated values of the overall Nonlinear part show that the estimated values generally follow the true values, with some deviations. The true and estimated values of f1 and f2 exhibit similar patterns, though the estimated values deviate from the true values at certain points. The error analysis between the true and estimated values reveals different trends. The error $f_1 - \hat{f}_1$ starts high, drops to near zero around 5 seconds, and remains low thereafter, indicating a quick convergence and consistent accuracy. The error $f_2 - \hat{f}_2$ increases to a peak around 10 seconds before decreasing back towards zero. The error $f_3 - \hat{f}_3$ shows a sharp peak around 5 seconds, followed by a gradual decrease. The projection algorithm effectively estimates the nonlinear components of the vehicle's dynamics, with the estimated values closely following the true values despite some deviations. This analysis confirms the algorithm's potential for accurately predicting nonlinear dynamics, essential for improving control in EVs.

The large estimation error during the transient interval for estimating the function f_1 is influenced by the learning rate η of the adaptation laws in equation (32). Specifically, a larger η results in greater estimation errors. This adjustment involved appropriately reducing η to minimize the estimation error while maintaining the desired closed-loop performance.

Fig. 7 illustrates the output power of the L1 adaptive control. Initially, the power output starts at a high value of around 3800 watts, then rapidly drops in a curved manner, forming a peak at the beginning, representing a burst of energy release.

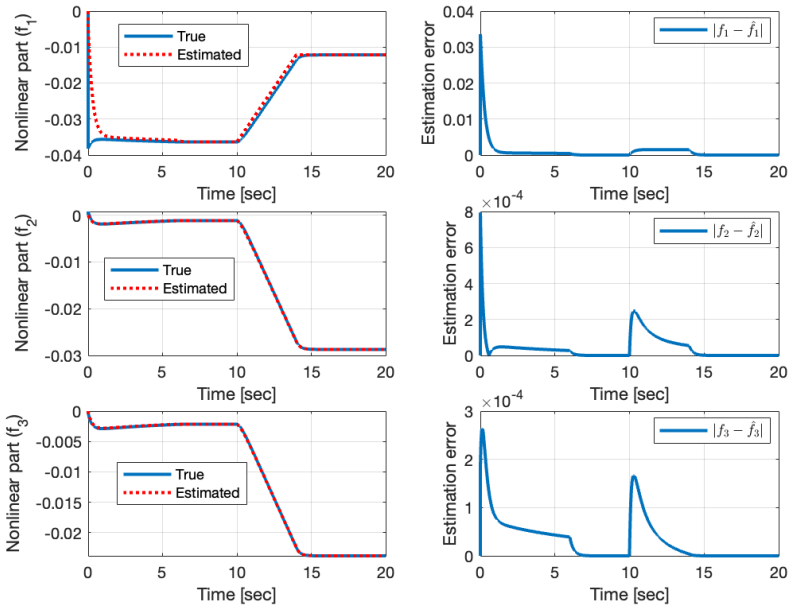

Fig. 6: True and estimated nonlinear parts of the EV dynamics.

Following this, the power output decreases and stabilizes at a lower level, around 1200 watts, indicating a steady-state operational phase. Towards the end, the power output gradually decreases further, forming a curved tail that approaches a low, steady value of around 200 to 300 watts, representing a low-power mode. The curve resembles an exponential decay or a power-up and power-down cycle, common in various EVs.

In the following, we evaluate the robustness of the proposed algorithm under conditions of measurement noise and external disturbances. Figure 8 presents the simulation results of the closed-loop adaptive control system with measurement noise affecting the output of the electric vehicle (EV) dynamics. For the simulation, we used white noise with standard deviations of 0.005 for the first state and 0.001 for the other two states. With this noise present, the virtual control signals fluctuate during both the transient and steady-state periods, leading to rapid changes in the torque signals. Despite these fluctuations, the maximum amplitude of the control signals remains within the normal range observed under standard conditions. Regarding the projection algorithm, the estimator can approximate the nonlinear parts of the EV dynamics, although it shows rapid variations around the true dynamics. Similarly, the output power follows a pattern similar to that under normal conditions, but it varies over time around the nominal values, deviating by up to 150 W from the nominal value.

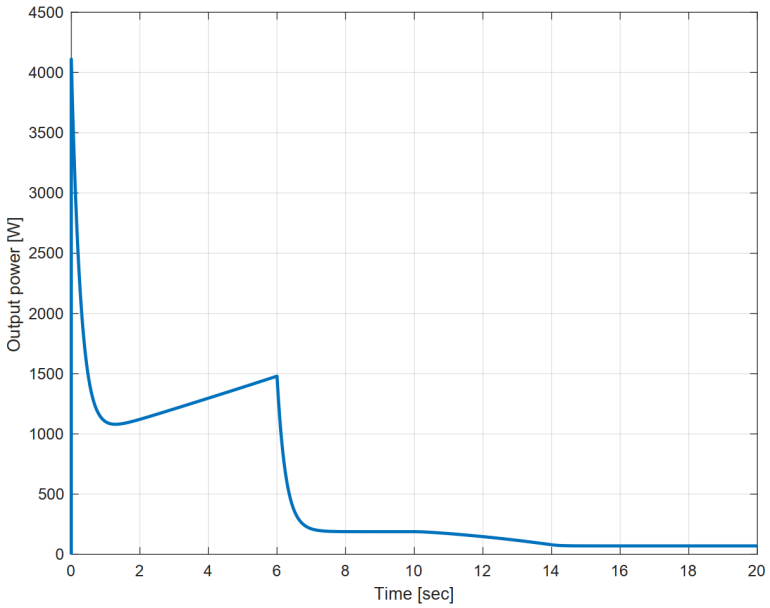

Fig. 7: Output power obtained by the proposed L1 adaptive control.

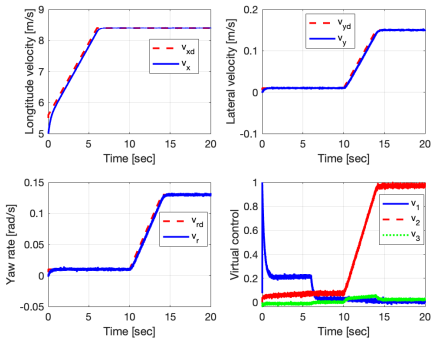

(a) Tracking control outcomes and virtual controls

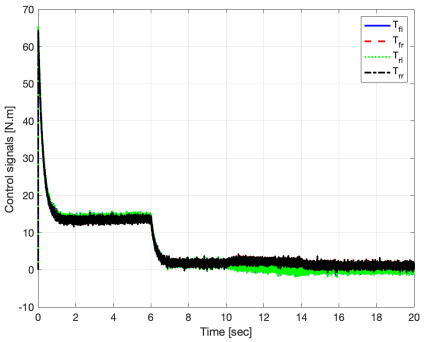

(b) Torque signals

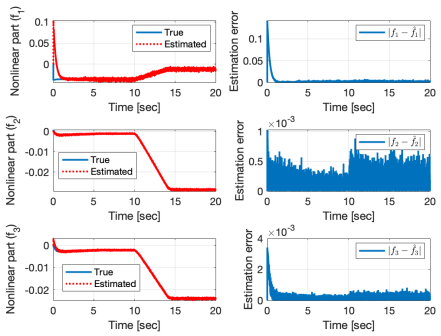

(c) True and estimated nonlinear parts

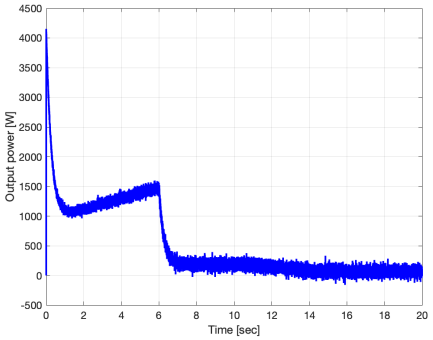

(d) Output power

Fig. 8: Simulation results of the proposed control algorithm in the presence of measurement noise.

Figure 9 shows the simulation results of the proposed algorithm under the influence of external disturbances. A step disturbance with an amplitude of 0.5 for the first state and 0.05 for the other two states is applied from 8 seconds to 11 seconds. The tracking motion shows deviations when the disturbance occurs, but it gradually converges back to the desired trajectory. The torque signals exhibit significant and rapid variations when the disturbance starts and stops, with amplitudes similar to those seen in the transient response. The external disturbance also affects the projection estimator, causing relatively large variations at the onset and end of the disturbance. Similarly, the output power experiences significant overshoots and undershoots when the disturbance begins and ends. The results indicate that a relatively large disturbance can considerably increase the energy required to counteract its effects. Overall, the algorithm is capable of maintaining its performance when the disturbance occurs.

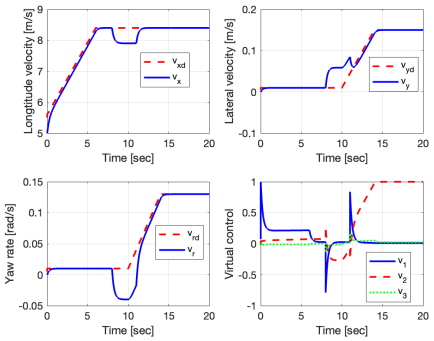

(a) Tracking control outcomes and virtual controls

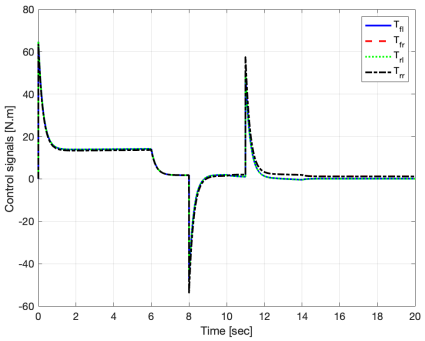

(b) Torque signals

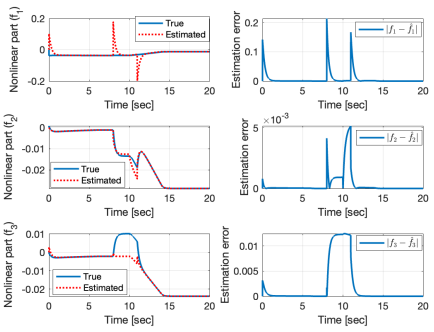

(c) True and estimated nonlinear parts

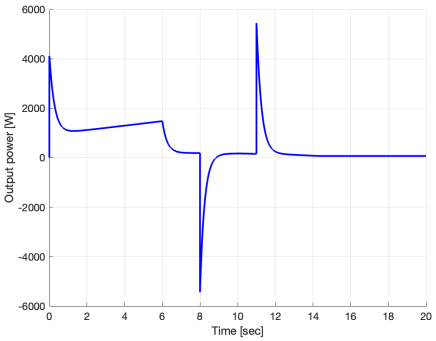

(d) Output power

Fig. 9: Simulation results of the proposed control algorithm in the presence of external step disturbance.

Another reference trajectory for the motion tracking of the vehicle is described below:

$$
\begin{aligned}
v_{xr} &= \begin{cases} 8.4 - 0.52(t-15), & \text{if } t > 15 \\ 8.4, & \text{else} \end{cases} \\
v_{yr} &= \begin{cases} 0.22 \sin\left(\frac{2\pi(t-5)}{5}\right), & \text{if } 5 < t \leq 10 \\ 0.01, & \text{else} \end{cases} \\
r_r &= \begin{cases} 0.23 \sin\left(\frac{2\pi(t-5)}{5}\right), & \text{if } 5 < t \leq 10 \\ 0.01, & \text{else} \end{cases}
\end{aligned} \tag{50}
$$

According to Fig. 10, the longitudinal velocity and the desired longitudinal velocity show a smooth trajectory as the velocity increases from a lower value towards the desired velocity. The lateral velocity and desired lateral velocity exhibit a sinusoidal-like oscillation, indicating a steering manoeuvre. The yaw rate and desired yaw rate also show a sinusoidal pattern, synchronized with the lateral velocity, indicating a coordinated turning motion.

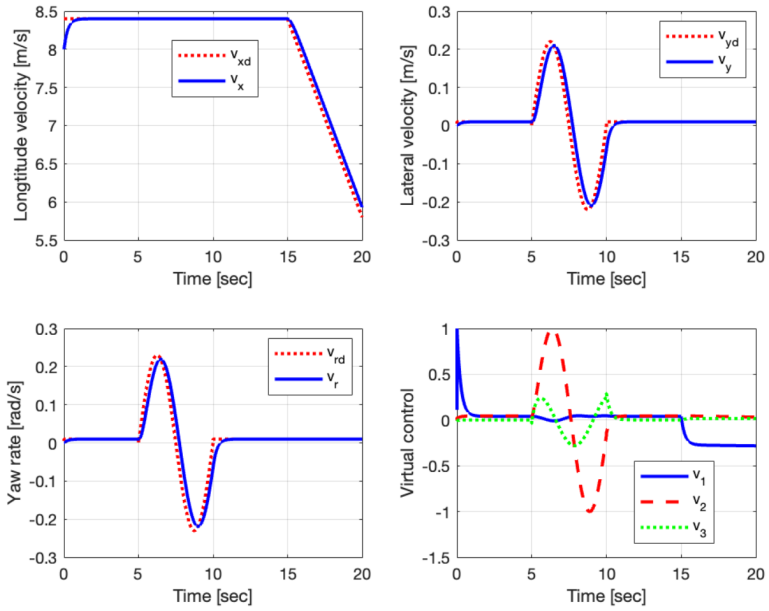

Fig. 10: Tracking control outcomes and virtual control signals (second maneuver).

The virtual control signals vary in correlation with the changes in the kinematic quantities, indicating the control actions being applied to achieve the desired motion. The results represent the behaviour of the proposed closed-loop vehicle executing a

maneuver involving longitudinal acceleration, lateral oscillations, and coordinated yaw rate adjustments, with the control signals modulated to track the desired kinematic trajectories while maintaining stability and control.

Fig. 11 shows the variation of torque signals generated by the proposed control algorithm to achieve vehicle planar motion tracking control over time. The four distinct torque signals display periodic, oscillating patterns, indicating active adjustments by the control system. Each signal exhibits unique frequency, phase, and magnitude characteristics, reflecting the different responses necessary for maintaining precise vehicle motion. The smooth, wave-like shapes of some signals indicate gradual adjustments, while others show more pronounced oscillations.

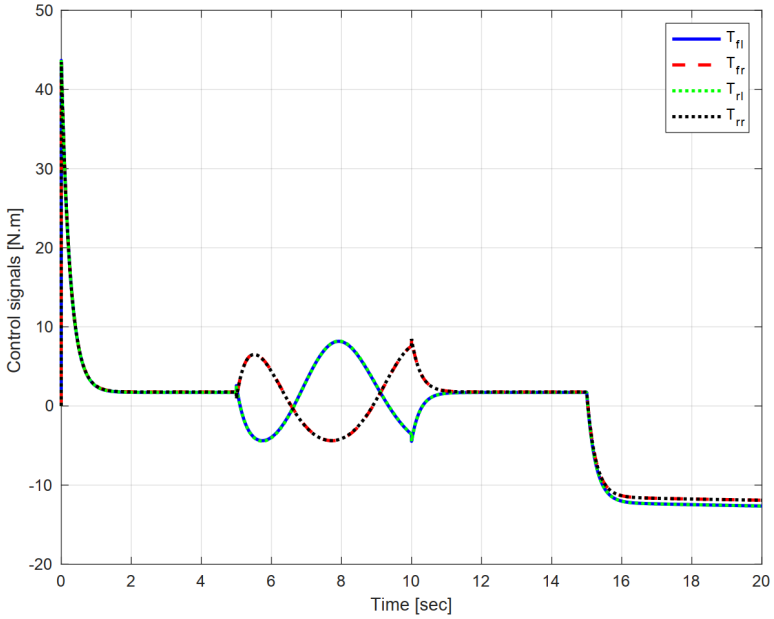

Fig. 11: Torque signals during the second maneuver of the EV using the proposed method.

Based on Fig. 12, a comparison of the true and estimated nonlinear parts of the EV dynamics shows a close match, indicating a robust estimation performance. Although, the estimation errors over time reveals periodic peaks, the magnitude of the errors is very small.

The singularity in estimating the functions f_2 and f_3 is due to the fact that the desired references for lateral velocity and yaw rate have zero crossing points, which cause relatively large variations at these points. Regarding the singularities, the proposed method cannot completely avoid large variations when the desired signals have zero-crossing stages. However, by fine-tuning the learning rate in the adaptation law,

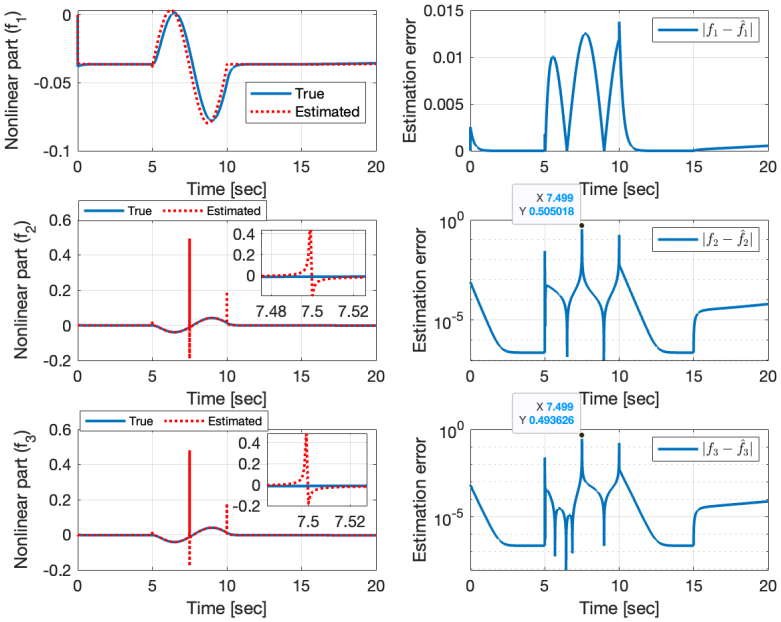

Fig. 12: True and estimated nonlinear parts of the EV dynamics.

lower variations can be achieved. Despite these variations, the projection algorithm effectively dampened them quickly.

Similar to the first manoeuvre, Fig. 13 depicts the power output profile of the closed-loop L1 adaptive control system. Initially, there is a sharp rise in power output, reaching a peak of approximately 4500 watts within the first few seconds, indicating a surge in power demand during system startup. Following this peak, the power output remains relatively high, fluctuating between 1000 and 1500 watts for an extended period, showing a consistent energy demand. Around 8 to 10 seconds, there is a notable decrease in power output, dropping to levels of around 200 to 400 watts, indicative of a transition to a lower power mode. Towards the end of the timeframe, between 16 and 18 seconds, there is a slight increase in power output, signifying a transient event before returning to a lower steady-state level.

In the simulation, we demonstrated that the projection-based adaptation laws effectively estimate the nonlinear components of EV dynamics. We illustrated this by showing the estimated nonlinearities for two different driving maneuvers. By accurately identifying these nonlinearities, the adaptive control strategy counteracts their effects on the closed-loop responses. Additionally, state feedback control maintains internal stability, while the feedforward term reduces steady-state error. This combined approach effectively addresses model uncertainty and external disturbances in EV dynamics.

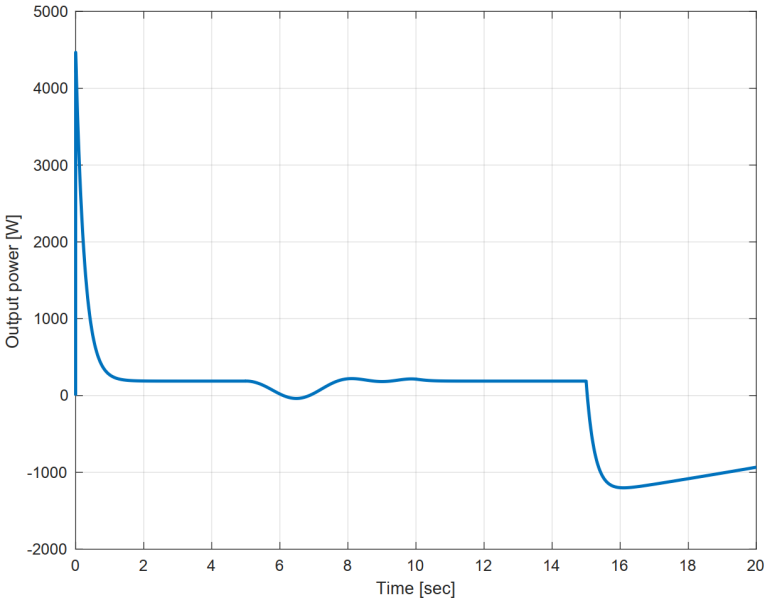

Fig. 13: Output power obtained by the proposed L1 adaptive control.

To analytically validate the robustness of the proposed method, we first represent the EV dynamics using a state-space model that separates the linear and nonlinear components. We define an unknown parametric matrix $f = B\theta^T x$ and derive two distinct adaptation laws for estimating f. The first law is based on Lyapunov theory, and the second utilizes L1 theory in conjunction with a projection operator.

Overall, these adaptation laws effectively mitigate the negative impact of the nonlinear components on the closed-loop response, demonstrating the method's robustness against model uncertainty in nonlinear EV dynamics. By decomposing the EV dynamics into linear and nonlinear parts, the state feedback control and feedforward gain are employed to handle the linear components, ensuring internal stability and minimizing steady-state error.

In the following, the performance of the proposed algorithm has been compared to the conventional MRAC and a new robust control method called Super Twisting Sliding Mode Control presented in [40]. To show the strength of the proposed method against two other methods, it is assumed that an unstructured uncertainty indicating 30% variation is occurred after 10 seconds in the nonlinear parts of the EV dynamics is considered.

Fig. 14 compares the performance the proposed LAC, MRAC, and STSMC. In terms of longitudinal velocity profiles, the proposed LAC and MRAC exhibit similar trajectories, while STSMC displays slightly different behavior. Regarding lateral velocity and yaw rate, Proposed LAC shows a smoother and more stable profile compared to MRAC and STSMC, which two other methods exhibit deviation with respect to the desired trajectory. All virtual controls vary between zero and one. The first

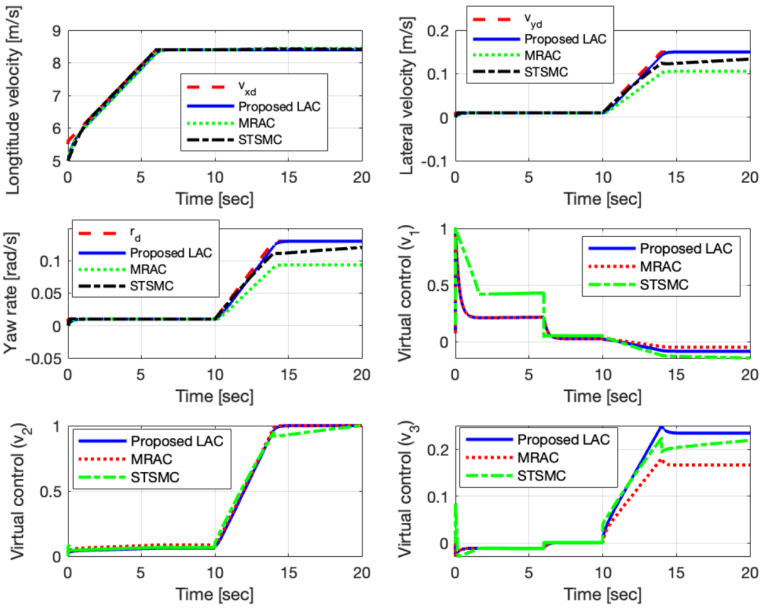

Fig. 14: Tracking control outcomes and virtual control signals for the proposed L1 adaptive control, MRAC, and STSMC [40].

virtual control of STSMC has more variations before occurring the uncertainty, while the third virtual control of MRAC and STSMC have less amplitude compared to the proposed control method.

Fig. 15 presents the control signal profiles of the proposed LAC, MRAC, and STSMC. The control signals initially exhibit high values across all methods, with the proposed LAC reaching the highest peak around 80 N.m. Over time, these signals gradually decrease and settle to lower steady-state values, with the proposed LAC and MRAC converging to a similar level, while STSMC settles at a slightly higher value.

This observation indicates that the proposed LAC may require a higher initial control effort to overcome disturbances, eventually converging to a steady-state input comparable to MRAC. Conversely, STSMC exhibits a slightly higher sustained control effort. These differences in control signal profiles reflect the distinct performance characteristics and behaviors of the three methods in terms of tracking reference trajectories, and rejecting disturbances. The proposed method requires slightly more energy than the super twisting method, particularly during the initial movement. However, it offers a smoother response, reduced steady-state error, and improved robustness compared to the super twisting method.

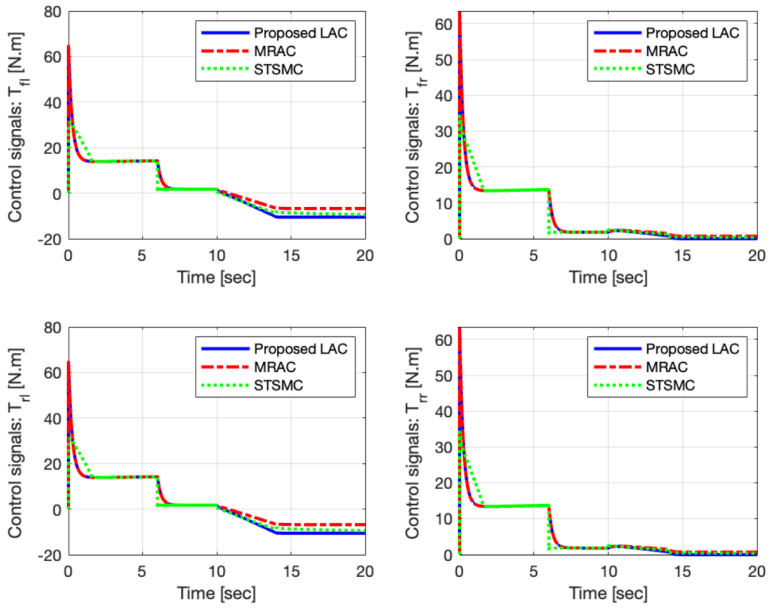

Fig. 15: Torque signals during the second maneuver of the EV using the proposed L1 adaptive control, MRAC, and STSMC [40].

Fig. 16 illustrates the output power profiles of the proposed LAC, MRAC, and STSMC. Initially, all methods experience a rapid surge in output power, with STSMC peaking at approximately 4500 watts within the first few seconds, representing a startup phase. Following this peak, MRAC and the proposed LAC demonstrate relatively lower and steadier power outputs compared to STSMC, which continues to exhibit higher oscillations. Around 6 to 8 seconds, all methods experience a gradual decrease in power output, with STSMC showing the most pronounced drop, followed by MRAC and the proposed LAC. Beyond 10 seconds, power outputs of all methods converge to a low, steady-state level, with the proposed LAC displaying the lowest power output among the three.

Overall, the power profiles indicate that while STSMC may have higher transient power demands, it shows less efficiency in maintaining a steady low-power state. Conversely, the proposed LAC and MRAC demonstrate better power management, with lower initial peaks and smoother transitions to sustained low-power output levels.

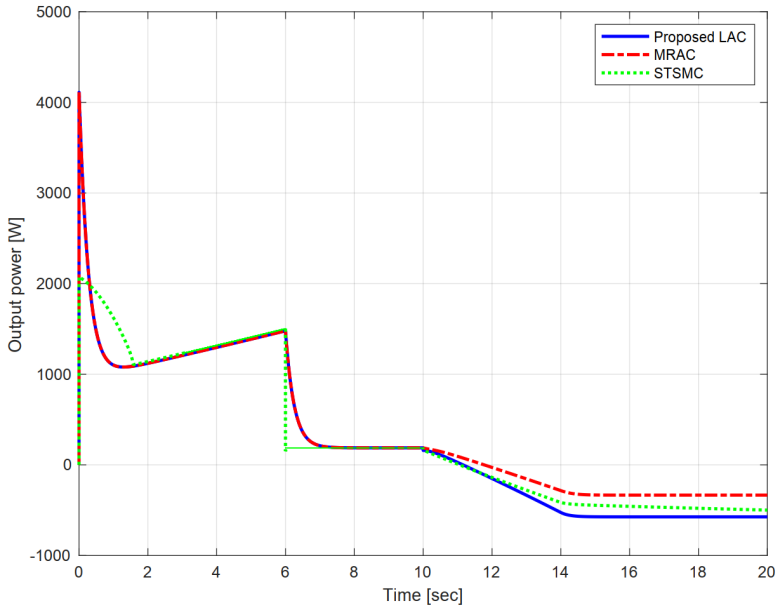

Fig. 16: Output power obtained by the proposed L1 adaptive control, MRAC and STSMC [40].

6 Conclusion

This study presented a robust adaptive control strategy based on $\mathcal{L}1$ theory and Lyapunov stability for the motion control of a four-wheel electric vehicle. By decomposing the vehicle dynamics into linear and nonlinear components, the proposed control method effectively managed the interaction between these aspects to achieve precise motion control. The inclusion of a reference model and a projection algorithm for estimating the nonlinear components further enhanced the performance of the control system. The proposed method ensured internal stability and minimized steady-state responses. The ability of the proposed method to accurately track various maneuvers was demonstrated through simulation results. The main advantage of the proposed method lies in the projection algorithm, which can estimate the nonlinear parts of the EV dynamics quickly and accurately. It was shown that the method maintains acceptable performance in the presence of noise and disturbances. Through rigorous evaluation and comparison with conventional model reference adaptive control and a recent control approach, the effectiveness and robustness of the proposed method against uncertainties inherent in the nonlinear aspects of vehicle dynamics were demonstrated. The proposed method provided a smoother and more stable response profile.

References

[1] Chan, C. C., Bouscayrol, A. & Chen, K. Electric, hybrid, and fuel-cell vehicles: Architectures and modeling. *IEEE transactions on vehicular technology* **59**, 589–598 (2009).

[2] Hardman, S., Chandan, A., Tal, G. & Turrentine, T. The effectiveness of financial purchase incentives for battery electric vehicles–a review of the evidence. *Renewable and Sustainable Energy Reviews* **80**, 1100–1111 (2017).

[3] Liu, W., Placke, T. & Chau, K. Overview of batteries and battery management for electric vehicles. *Energy Reports* **8**, 4058–4084 (2022).

[4] Mitra, D., Ghosh, S. & Mukhopadhyay, S. Model-based estimation of state of charge and state of power of a lithium ion battery pack and their effects on energy management in hybrid electric vehicles. *International Journal of Dynamics and Control* **12**, 2033–2049 (2024).

[5] Najjaran, S., Rahmani, Z. & Hassanzadeh, M. Fuzzy predictive control strategy for plug-in hybrid electric vehicles over multiple driving cycles. *International Journal of Dynamics and Control* **10**, 930–941 (2022).

[6] Zhang, L. *et al.* An adaptive backstepping sliding mode controller to improve vehicle maneuverability and stability via torque vectoring control. *IEEE Transactions on Vehicular Technology* **69**, 2598–2612 (2020).

[7] Ammari, O., El Majdoub, K., Giri, F. & Baz, R. Nonlinear control of a half electric vehicle including an inverter, an in-wheel bldc motor and pacejka's tire model. *International Journal of Dynamics and Control* 1–13 (2024).

[8] Rahman, A. U., Ahmad, I. & Malik, A. S. Variable structure-based control of fuel cell-supercapacitor-battery based hybrid electric vehicle. *Journal of Energy Storage* **29**, 101365 (2020).

[9] Chen, J., Shuai, Z., Zhang, H. & Zhao, W. Path following control of autonomous four-wheel-independent-drive electric vehicles via second-order sliding mode and nonlinear disturbance observer techniques. *IEEE Transactions on Industrial Electronics* **68**, 2460–2469 (2020).

[10] Rahman, A. U., Zehra, S. S., Ahmad, I. & Armghan, H. Fuzzy supertwisting sliding mode-based energy management and control of hybrid energy storage system in electric vehicle considering fuel economy. *Journal of Energy Storage* **37**, 102468 (2021).

[11] Mei, P., Karimi, H. R., Yang, S., Xu, B. & Huang, C. An adaptive fuzzy sliding-mode control for regenerative braking system of electric vehicles. *International Journal of Adaptive Control and Signal Processing* **36**, 391–410 (2022).

[12] He, L., Ye, W., He, Z., Song, K. & Shi, Q. A combining sliding mode control approach for electric motor anti-lock braking system of battery electric vehicle. *Control Engineering Practice* **102**, 104520 (2020).

[13] Wang, R. *et al.* Vehicle-vehicle energy interaction converter of electric vehicles: A disturbance observer based sliding mode control algorithm. *IEEE Transactions on Vehicular Technology* **70**, 9910–9921 (2021).

[14] Liang, Z., Zhao, J., Dong, Z., Wang, Y. & Ding, Z. Torque vectoring and rear-wheel-steering control for vehicle's uncertain slips on soft and slope terrain using

sliding mode algorithm. *IEEE Transactions on Vehicular Technology* **69**, 3805–3815 (2020).

[15] Zhang, J. *et al.* Active front steering-based electronic stability control for steer-by-wire vehicles via terminal sliding mode and extreme learning machine. *IEEE Transactions on Vehicular Technology* **69**, 14713–14726 (2020).

[16] Hu, Y. & Wang, H. Robust tracking control for vehicle electronic throttle using adaptive dynamic sliding mode and extended state observer. *Mechanical Systems and Signal Processing* **135**, 106375 (2020).

[17] Sreejith, R. & Singh, B. Sensorless predictive control of spmsm-driven light ev drive using modified speed adaptive super twisting sliding mode observer with maf-pll. *IEEE Journal of Emerging and Selected Topics in Industrial Electronics* **2**, 42–52 (2020).

[18] Wang, X. & Suh, C. S. Nonlinear time-frequency control of pm synchronous motor instability applicable to electric vehicle application. *International Journal of Dynamics and Control* **4**, 400–412 (2016).

[19] Muhammad, E., Vali, A., Kashaninia, A. & Bahnamgol, V. Stability enhancement of hybrid electric vehicles using optimal fuzzy logic. *International Journal of Dynamics and Control* **12**, 1130–1145 (2024).

[20] Pan, C., Zhang, C., Wang, J. & Liu, Q. Adaptive cruise control strategy for electric vehicles considering battery degradation characteristics. *Applied Sciences* **13**, 4553 (2023).

[21] Ma, H., Chu, L., Guo, J., Wang, J. & Guo, C. Cooperative adaptive cruise control strategy optimization for electric vehicles based on sa-pso with model predictive control. *IEEE Access* **8**, 225745–225756 (2020).

[22] Jia, Y., Jibrin, R. & Görges, D. Energy-optimal adaptive cruise control for electric vehicles based on linear and nonlinear model predictive control. *IEEE Transactions on Vehicular Technology* **69**, 14173–14187 (2020).

[23] Peng, C. & Chen, L. Model reference adaptive control based on adjustable reference model during mode transition for hybrid electric vehicles. *Mechatronics* **87**, 102894 (2022).

[24] Elzaghir, W., Zhang, Y., Natarajan, N., Massey, F. & Mi, C. C. Model reference adaptive control for hybrid electric vehicle with dual clutch transmission configurations. *IEEE Transactions on Vehicular Technology* **67**, 991–999 (2017).

[25] Hovakimyan, N. & Cao, C. *$\mathcal{L}1$ adaptive control theory: Guaranteed robustness with fast adaptation* (SIAM, 2010).

[26] Astrom, K. & Wittenmark, B. Adaptive control. courier corporation. *Courier Corporation* **3** (2013).

[27] Cao, C. & Hovakimyan, N. Design and analysis of a novel l1 adaptive controller, part i: Guaranteed transient performance 3403–3408 (2006).

[28] Cao, C. & Hovakimyan, N. Design and analysis of a novel l1 adaptive controller, part ii: Guaranteed transient performance 3403–3408 (2006).

[29] Mallikarjunan, S. *et al.* L1 adaptive controller for attitude control of multirotors 4831 (2012).

[30] Lakshmanan, A., Gahlawat, A. & Hovakimyan, N. Safe feedback motion planning: A contraction theory and l1 adaptive control based approach 1578–1583 (2020).

[31] Ghodbane, A., Madali, A.-S., Bensoussan, D. & Hammami, M. Comparative study between l1 adaptive controller and bl1 adaptive controller. *2022 10th International Conference on Systems and Control (ICSC)* 329–333 (2022).

[32] Boubakir, A., Labiod, S. & Boudjerda, N. Robust l1 fuzzy adaptive controller for three-phase grid-connected photovoltaic system. *Journal of the Franklin Institute* **359**, 1852–1880 (2022).

[33] Xu, H., Oliveira, P. & Soares, C. G. L1 adaptive backstepping control for path-following of underactuated marine surface ships. *European Journal of Control* **58**, 357–372 (2021).

[34] Thu, K. M. & Gavrilov, A. Designing and modeling of quadcopter control system using l1 adaptive control. *Procedia Computer Science* **103**, 528–535 (2017).

[35] Lee, J. & Smith, J. L1 adaptive control for safety-critical systems. *IEEE Transactions on Automatic Control* **57**, 150–165 (2012).

[36] Michini, B. & Smith, J. L1 adaptive control for flexible spacecraft. *AIAA Guidance, Navigation, and Control Conference* 1–12 (2009).

[37] Wang, J., Patel, V. V., Cao, C., Hovakimyan, N. & Lavretsky, E. Novel l1 adaptive control methodology for aerial refueling with guaranteed transient performance. *Journal of guidance, control, and dynamics* **31**, 182–193 (2008).

[38] Chen, Y. & Wang, J. Adaptive energy-efficient control allocation for planar motion control of over-actuated electric ground vehicles. *IEEE Transactions on Control Systems Technology* **22**, 1362–1373 (2013).

[39] Chen, Y. & Wang, J. Design and evaluation on electric differentials for over-actuated electric ground vehicles with four independent in-wheel motors. *IEEE Transactions on Vehicular Technology* **61**, 1534–1542 (2012).

[40] Chen, Q. *et al.* Afs control system research of distributed drive electric vehicles by adaptive super-twisting sliding mode control. *Transactions of the Institute of Measurement and Control* **46**, 1388–1396 (2024).